APPENDIX

APPENDIX A: MULTI-TIME HIGHER-ORDER RESPONSE AND GENERALIZED PARAMETER-SHIFT RULE

This appendix derives a unified bridge from multi-time, higher-order response theory to the generalized parameter-shift rule (GPSR) used in our circuit implementations. We start from the interaction-picture Kubo expansion: the mth-order response kernel is a nested-commutator object with explicit causality. We then recast the response as derivatives of a generating functional with respect to the driving fields. Restricting the drive to a finite set of δ-pulses reduces the functional dependence on continuous fields to an ordinary dependence on a finite parameter vector $\vec{\eta}$ that is directly programmable on hardware. When each pulse generator has a finite discrete spectrum, the generating function becomes a finite Fourier series in the corresponding control parameter(s), which enables an exact GPSR: any (mixed) derivative at $\vec{\eta} = \vec{0}$ can be reconstructed from finitely many shifted evaluations at discrete parameter configurations. This provides an experimentally accessible route from formal higher-order response theory to finite-shot estimation on quantum devices.

A.1 General form of the response function

We consider an unperturbed Hamiltonian $\mathbf{H}_0$ and an observable $\mathbf{A}$. In the interaction picture,

$$\mathbf{A}(t) = U_0^\dagger(t)\,\mathbf{A}\,U_0(t), \qquad U_0(t) = e^{-i\mathbf{H}_0 t}. \tag{13}$$

The system is driven by a weak, linearly coupled perturbation

$$\mathbf{H}_I(t) = \sum_a h_a(t)\,\mathbf{B}_a(t), \qquad \mathbf{B}_a(t) = U_0^\dagger(t)\,\mathbf{B}_a\,U_0(t), \tag{14}$$

where a labels a finite set of drive "channels" (e.g., different polarization/spin components or different Pauli strings in circuits). The initial state is a (possibly mixed) density matrix

$$\boldsymbol{\rho}_0, \qquad \langle X\rangle_0 := \mathrm{Tr}(X\boldsymbol{\rho}_0). \tag{15}$$

We use the commutator superoperator

$$\mathrm{ad}_X(Y) = [X, Y]. \tag{16}$$

In the interaction picture, the density matrix satisfies

$$i\,\frac{d}{dt}\boldsymbol{\rho}_I(t) = [\mathbf{H}_I(t), \boldsymbol{\rho}_I(t)], \qquad \boldsymbol{\rho}_I(t_0) = \boldsymbol{\rho}_0. \tag{17}$$

Taking $t_0 \to -\infty$, the integral equation reads

$$\boldsymbol{\rho}_I(t) = \boldsymbol{\rho}_0 - i\int_{-\infty}^{t} dt_1\,[\mathbf{H}_I(t_1), \boldsymbol{\rho}_I(t_1)]. \tag{18}$$

Iterating Eq. (18) yields the Dyson series. In general, the mth-order contribution is

$$\boldsymbol{\rho}_I^{(m)}(t) = (-i)^m \int_{-\infty}^{t} dt_1 \int_{-\infty}^{t_1} dt_2 \cdots \int_{-\infty}^{t_{m-1}} dt_m\ \mathrm{ad}_{\mathbf{H}_I(t_1)} \cdots \mathrm{ad}_{\mathbf{H}_I(t_m)}\,\boldsymbol{\rho}_0. \tag{19}$$

Using step functions, the nested limits in Eq. (19) can be recast as

$$\int_{-\infty}^{t} dt_1 \int_{-\infty}^{t_1} dt_2 \cdots \int_{-\infty}^{t_{m-1}} dt_m = \int dt_1 \cdots dt_m\,\theta(t-t_1)\theta(t_1-t_2)\cdots\theta(t_{m-1}-t_m). \tag{20}$$

Thus

$$\boldsymbol{\rho}_I(t) - \boldsymbol{\rho}_0 = \sum_{m=1}^{\infty}(-i)^m \int dt_1 \cdots dt_m\,\theta(t-t_1)\cdots\theta(t_{m-1}-t_m)\ \mathrm{ad}_{\mathbf{H}_I(t_1)} \cdots \mathrm{ad}_{\mathbf{H}_I(t_m)}\,\boldsymbol{\rho}_0. \tag{21}$$

The induced deviation of $\langle \mathbf{A}(t)\rangle$ is

$$\delta\langle \mathbf{A}(t)\rangle = \mathrm{Tr}\{\mathbf{A}(t)[\boldsymbol{\rho}_I(t) - \boldsymbol{\rho}_0]\}. \tag{22}$$

Substituting Eq. (21) into Eq. (22) gives

$$\delta\langle \mathbf{A}(t)\rangle = \sum_{m=1}^{\infty} (-i)^m \int dt_1 \cdots dt_m\, \theta(t-t_1)\cdots\theta(t_{m-1}-t_m)\, \mathrm{Tr}\{\mathbf{A}(t)\ \mathrm{ad}_{\mathbf{H}_I(t_1)}\cdots \mathrm{ad}_{\mathbf{H}_I(t_m)}\,\boldsymbol{\rho}_0\}. \tag{23}$$

We now use the trace identity

$$\mathrm{Tr}\{X[Y,\boldsymbol{\rho}_0]\} = \mathrm{Tr}\{[X,Y]\boldsymbol{\rho}_0\}, \tag{24}$$

which moves commutators from $\boldsymbol{\rho}_0$ onto $\mathbf{A}(t)$. By induction,

$$\mathrm{Tr}\{\mathbf{A}\ \mathrm{ad}_{\mathbf{H}_I(t_1)}\cdots \mathrm{ad}_{\mathbf{H}_I(t_m)}\,\boldsymbol{\rho}_0\} = (-1)^m\, \mathrm{Tr}\{\mathrm{ad}_{\mathbf{H}_I(t_m)}\cdots \mathrm{ad}_{\mathbf{H}_I(t_1)}\,\mathbf{A}\,\boldsymbol{\rho}_0\}. \tag{25}$$

Inserting Eq. (25) into Eq. (23) yields the causal (time-ordered) Kubo form

$$\delta\langle \mathbf{A}(t)\rangle = \sum_{m=1}^{\infty} i^m \int dt_1 \cdots dt_m\, \theta(t-t_1)\cdots\theta(t_{m-1}-t_m)\, \big\langle\, \mathrm{ad}_{\mathbf{H}_I(t_m)}\cdots \mathrm{ad}_{\mathbf{H}_I(t_1)}\,\mathbf{A}(t)\big\rangle_0. \tag{26}$$

Expanding $\mathbf{H}_I(t_k) = \sum_{a_k} h_{a_k}(t_k)\mathbf{B}_{a_k}(t_k)$ in Eq. (26), we obtain the standard response expansion

$$\delta\langle \mathbf{A}(t)\rangle = \sum_{m=1}^{\infty} \sum_{a_1,\ldots,a_m} \int dt_1 \cdots dt_m\, \chi^{(m)}_{\mathbf{A};a_1\cdots a_m}(t;t_1,\ldots,t_m) \prod_{k=1}^{m} h_{a_k}(t_k), \tag{27}$$

with the causal mth-order kernel

$$\boxed{\chi^{(m)}_{\mathbf{A};a_1\cdots a_m}(t;t_1,\ldots,t_m) = i^m\,\theta(t-t_1)\cdots\theta(t_{m-1}-t_m)\,\big\langle\, \mathrm{ad}_{\mathbf{B}_{a_m}(t_m)}\cdots \mathrm{ad}_{\mathbf{B}_{a_1}(t_1)}\,\mathbf{A}(t)\big\rangle_0.} \tag{28}$$

The Fourier transform (convention $f(\omega) = \int dt\, e^{i\omega t} f(t)$) is

$$\chi^{(m)}_{\mathbf{A};a_1\cdots a_m}(\omega_1,\ldots,\omega_m) = \int dt_1 \cdots dt_m\, e^{i\sum_k \omega_k t_k}\, \chi^{(m)}_{\mathbf{A};a_1\cdots a_m}(t;t_1,\ldots,t_m), \tag{29}$$

which enters nonlinear spectra such as multidimensional spectroscopy.

For a given field configuration $\vec{h} = \{h_a(t)\}$, define the generating functional

$$\mathcal{G}_{\mathbf{A}}[\vec{h};t] \equiv \langle \mathbf{A}(t)\rangle_{\vec{h}}. \tag{30}$$

Formally expanding around $\vec{h} = \vec{0}$ gives

$$\mathcal{G}_{\mathbf{A}}[\vec{h};t] - \langle \mathbf{A}(t)\rangle_0 = \sum_{m=1}^{\infty} \frac{1}{m!} \sum_{a_1,\ldots,a_m} \int dt_1 \cdots dt_m\, \Gamma^{(m)}_{\mathbf{A};a_1\cdots a_m}(t;t_1,\ldots,t_m) \prod_{k=1}^{m} h_{a_k}(t_k), \tag{31}$$

where

$$\Gamma^{(m)}_{\mathbf{A};a_1\cdots a_m}(t;t_1,\ldots,t_m) = \left.\frac{\delta^m \langle \mathbf{A}(t)\rangle_{\vec{h}}}{\delta h_{a_1}(t_1)\cdots\delta h_{a_m}(t_m)}\right|_{\vec{h}=\vec{0}}. \tag{32}$$

The $m!$ and the precise symmetry of $\Gamma^{(m)}$ depend on whether one treats $(t_1,\ldots,t_m)$ as unordered arguments (fully symmetric functional derivatives) or restricts to an explicit time-ordered sector (where no combinatorial factor appears). Throughout this appendix, we keep the causal Kubo kernel $\chi^{(m)}$ in Eq. (28) as the primary object, and use Eq. (32) only as a device to connect response coefficients to derivatives of a finite-dimensional parameter function under δ-pulse drives (Sec. 3).

A.2 δ-pulse restriction and finite-dimensional parameterization

We now restrict the drive to a finite set of δ-pulses, as implemented in our circuits. Throughout the paper we group pulses into L drive channels labeled by $a \in \{0, 1, \ldots, L-1\}$. Channel a has a single programmable amplitude η_a but may contain multiple pulses at times $\{t_{ab}\}_{b=0}^{n_a-1}$:

$$\mathbf{H}_I(t) = \sum_{a=0}^{L-1} h_a(t)\, \mathbf{B}_a(t), \qquad h_a(t) = \eta_a \sum_{b=0}^{n_a-1} \delta(t - t_{ab}). \tag{33}$$

Under this δ-pulse restriction, the generating functional $\mathcal{G}_{\mathbf{A}}[\vec{h}; t]$ reduces to an ordinary function of the finite parameter vector $\vec{\eta} = (\eta_0, \ldots, \eta_{L-1})$:

$$\mathcal{G}_{\mathbf{A}}(\vec{\eta}; t) := \mathcal{G}_{\mathbf{A}}[\vec{h}^{(\vec{\eta})}; t] = \langle \mathbf{A}(t) \rangle_{\vec{\eta}}. \tag{34}$$

a. Response expansion under channel δ-pulses. Substituting Eq. (33) into the Volterra/Kubo expansion Eq. (27) gives a polynomial in $\{\eta_a\}$:

$$\delta\langle \mathbf{A}(t) \rangle = \sum_{m=1}^{\infty} \sum_{a_1, \ldots, a_m = 0}^{L-1} \left[\sum_{b_1=0}^{n_{a_1}-1} \cdots \sum_{b_m=0}^{n_{a_m}-1} \chi^{(m)}_{\mathbf{A}; a_1 \cdots a_m}\left(t; t_{a_1 b_1}, \ldots, t_{a_m b_m}\right) \right] \prod_{k=1}^{m} \eta_{a_k}. \tag{35}$$

b. β_a-counting and the correct Taylor prefactor. For a given term indexed by $(a_1, \ldots, a_m)$, define the multiplicities (occupation numbers)

$$\beta_a := \sum_{k=1}^{m} \delta_{a_k, a}, \qquad \sum_{a=0}^{L-1} \beta_a = m, \tag{36}$$

so that the monomial satisfies $\prod_{k=1}^{m} \eta_{a_k} = \prod_{a=0}^{L-1} \eta_a^{\beta_a}$. The multivariate Taylor expansion of $\mathcal{G}_{\mathbf{A}}(\vec{\eta}; t)$ around $\vec{\eta} = \vec{0}$ reads

$$\mathcal{G}_{\mathbf{A}}(\vec{\eta}; t) - \mathcal{G}_{\mathbf{A}}(\vec{0}; t) = \sum_{m=1}^{\infty} \sum_{\{\beta_a\}: \sum_a \beta_a = m} \frac{1}{\prod_{a=0}^{L-1} \beta_a!} \left(\prod_{a=0}^{L-1} \frac{\partial^{\beta_a}}{\partial \eta_a^{\beta_a}} \right) \mathcal{G}_{\mathbf{A}}(\vec{\eta}; t) \Big|_{\vec{\eta}=\vec{0}} \prod_{a=0}^{L-1} \eta_a^{\beta_a}. \tag{37}$$

Comparing Eq. (35) with Eq. (37), we obtain the key identification

$$\sum_{b_1=0}^{n_{a_1}-1} \cdots \sum_{b_m=0}^{n_{a_m}-1} \chi^{(m)}_{\mathbf{A}; a_1 \cdots a_m}\left(t; t_{a_1 b_1}, \ldots, t_{a_m b_m}\right) = \frac{1}{\prod_{a=0}^{L-1} \beta_a!} \left(\prod_{a=0}^{L-1} \frac{\partial^{\beta_a}}{\partial \eta_a^{\beta_a}} \right) \mathcal{G}_{\mathbf{A}}(\vec{\eta}; t) \Big|_{\vec{\eta}=\vec{0}}. \tag{38}$$

The only subtlety relative to the pulse-resolved convention is precisely this β_a-dependent prefactor. If every pulse carried an *independent* amplitude parameter (no identifications across channels), one would recover the familiar $1/m!$ prefactor.

A.3 Generalized parameter-shift representation of response functions

Single-parameter GPSR

We now connect the derivative form in Eq. (38) to GPSR. Consider a single-parameter expectation value

$$F(\eta) = \left\langle e^{i\eta \mathbf{B}}\, \mathbf{A}\, e^{-i\eta \mathbf{B}} \right\rangle_0, \tag{39}$$

where $\mathbf{B}$ is a bounded Hermitian operator with a finite discrete spectrum

$$\mathbf{B} = \sum_{s \in S} \lambda_s P_s, \qquad P_s P_{s'} = \delta_{s,s'} P_s, \quad \sum_s P_s = \mathbb{I}. \tag{40}$$

Inserting the spectral decomposition into Eq. (39) yields a finite Fourier series

$$F(\eta) = \sum_{s,s'} e^{i\eta(\lambda_s - \lambda_{s'})} \operatorname{Tr}\left[\boldsymbol{\rho}_0 P_s \mathbf{A} P_{s'}\right] = \sum_{\omega \in \Omega} \hat{F}(\omega)\, e^{i\omega\eta}, \tag{41}$$

with frequency set

$$\Omega := \{\lambda_s - \lambda_{s'} \mid s, s' \in S\}, \tag{42}$$

and coefficients

$$\hat{F}(\omega) := \sum_{(s,s'):\lambda_s - \lambda_{s'} = \omega} \operatorname{Tr}\left[\boldsymbol{\rho}_0 P_s \mathbf{A} P_{s'}\right]. \tag{43}$$

Therefore

$$F^{(r)}(0) = \sum_{\omega \in \Omega} \hat{F}(\omega)(i\omega)^r. \tag{44}$$

On hardware we estimate $F(\eta)$ at selected shifts $\{s_p\}_{p=1}^M$. We seek coefficients $\{c_p^{(r)}\}$ such that

$$F^{(r)}(0) = \sum_{p=1}^{M} c_p^{(r)}\, F(s_p). \tag{45}$$

Substituting Eq. (41) into Eq. (45) gives the linear system

$$\sum_{p=1}^{M} c_p^{(r)} e^{i\omega s_p} = (i\omega)^r, \qquad \forall \omega \in \Omega, \tag{46}$$

whose solution defines the GPSR rule. A minimal choice is typically $M \geq |\Omega|$ (with equality if the resulting Vandermonde-type matrix is invertible). As a special case, for a Pauli-type generator with spectrum $\{\pm 1/2\}$ one recovers the usual parameter-shift rule

$$F'(0) = \frac{F(\pi/2) - F(-\pi/2)}{2}. \tag{47}$$

Multi-parameter GPSR

We now extend GPSR to the multi-parameter generating function

$$\mathcal{G}_{\mathbf{A}}(\vec{\eta}; t) = \mathcal{G}_{\mathbf{A}}(\eta_0, \ldots, \eta_{L-1}; t), \qquad \vec{\eta} = (\eta_0, \ldots, \eta_{L-1}). \tag{48}$$

For each parameter η_a, the associated generator is $\mathbf{B}_a$ with finite discrete spectrum

$$\mathbf{B}_a = \sum_s \lambda_{a,s} P_{a,s}, \qquad \Omega_a := \{\lambda_{a,s} - \lambda_{a,s'}\}. \tag{49}$$

Choose shift points $\{s_{a,p}\}_{p=1}^{M_a}$ and solve the one-dimensional GPSR system

$$\sum_{p=1}^{M_a} c_{a,p}^{(r)} e^{i\omega s_{a,p}} = (i\omega)^r, \qquad \forall\, \omega \in \Omega_a, \tag{50}$$

which produces coefficients $c_{a,p}^{(r)}$ for each derivative order r.

For an order-m term characterized by the multiplicities $\{\beta_a\}$ in Eq. (36), the multi-parameter GPSR factorizes:

$$\left(\prod_{a=0}^{L-1} \frac{\partial^{\beta_a}}{\partial \eta_a^{\beta_a}}\right) \mathcal{G}_{\mathbf{A}}(\vec{\eta}; t)\Big|_{\vec{\eta}=\vec{0}} = \sum_{p_0=1}^{M_0} \cdots \sum_{p_{L-1}=1}^{M_{L-1}} \left[\prod_{a=0}^{L-1} c_{a,p_a}^{(\beta_a)}\right] \mathcal{G}_{\mathbf{A}}\big(\eta_0 = s_{0,p_0}, \ldots, \eta_{L-1} = s_{L-1,p_{L-1}}; t\big). \tag{51}$$

Combining Eq. (51) with Eq. (38) yields the GPSR estimator directly for the multi-pulse response coefficient in Eq. (35):

$$\sum_{b_1=0}^{n_{a_1}-1}\cdots\sum_{b_m=0}^{n_{a_m}-1}\chi^{(m)}_{\mathbf{A};a_1\cdots a_m}(t;t_{a_1b_1},\ldots,t_{a_mb_m})=\frac{1}{\prod_{a=0}^{L-1}\beta_a!}\sum_{p_0=1}^{M_0}\cdots\sum_{p_{L-1}=1}^{M_{L-1}}\left[\prod_{a=0}^{L-1}c_{a,p_a}^{(\beta_a)}\right]\mathcal{G}_{\mathbf{A}}\big(\eta_0=s_{0,p_0},\ldots,\eta_{L-1}=s_{L-1,p_{L-1}};t\big). \tag{52}$$

In summary, the nonlinear response kernels can be expressed either (i) as Kubo-type nested commutators with explicit causality (Eqs. (26) and (28)), or (ii) as derivatives of the finite-dimensional generating function at $\vec{\eta}=\vec{0}$ under δ-pulse drives. GPSR turns these derivatives into a finite linear combination of shifted expectation values, yielding an exact and hardware-friendly route to estimating higher-order response functions from finite-shot measurements.

APPENDIX B: COMPLEXITY ANALYSIS OF THE GENERALIZED PARAMETER-SHIFT RULE (GPSR)

This appendix provides a self-contained resource analysis for the generalized parameter-shift rule (GPSR) used to reconstruct multi-time higher-order responses (equivalently, high-order pump derivatives). We decompose the overall cost into: (i) the number of distinct circuit instances (shift configurations), and (ii) the sampling cost (shots) required to achieve an additive precision ϵ.

We consider an impulsive pump implemented by a unitary kick $e^{-i\eta\mathbf{B}}$ (single parameter) or a product of kicks $\prod_{a=0}^{L-1}e^{-i\eta_a\mathbf{B}_a}$ (multi-parameter). The experimentally measured observable is

$$F(\eta)\equiv\langle\mathbf{A}(t)\rangle_\eta=\langle e^{i\eta\mathbf{B}}\mathbf{A}(t)e^{-i\eta\mathbf{B}}\rangle_0, \tag{53}$$

or, in the multi-parameter setting,

$$\mathcal{G}_{\mathbf{A}}(\vec{\eta})\equiv\langle\mathbf{A}(t)\rangle_{\vec{\eta}},\qquad\vec{\eta}=(\eta_0,\ldots,\eta_{L-1}). \tag{54}$$

The goal of GPSR is to reconstruct the mixed derivative at $\vec{\eta}=\vec{0}$ from finitely many shifted evaluations:

$$\partial_{\vec{\eta}}^{\vec{\beta}}\mathcal{G}_{\mathbf{A}}(\vec{0}),\qquad\vec{\beta}=(\beta_0,\ldots,\beta_{L-1})\in\mathbb{N}^L, \tag{55}$$

where $\vec{\beta}$ is a multi-index taking non-negative integers.

B.1 Single-parameter GPSR: shift count and exactness

Finite spectrum ⇒ finite Fourier support

Assume that the generator $\mathbf{B}$ admits a finite discrete spectral decomposition,

$$\mathbf{B}=\sum_{s\in S}\lambda_sP_s, \tag{56}$$

where P_s are projection operators satisfying $\sum_{s\in S}P_s=I$ and $P_sP_{s'}=\delta_{s,s'}P_s$. Then the measured expectation value $F(\eta)$ has the corresponding decomposition

$$\begin{aligned}F(\eta)&=\mathrm{Tr}\big[\boldsymbol{\rho}_0\,e^{i\eta\mathbf{B}}\mathbf{A}(t)e^{-i\eta\mathbf{B}}\big]\\&=\sum_{s,s'\in S}e^{i\eta(\lambda_s-\lambda_{s'})}\,\mathrm{Tr}[\boldsymbol{\rho}_0P_s\mathbf{A}(t)P_{s'}]\,.\end{aligned} \tag{57}$$

Define the spectral-difference set

$$\Omega=\{\lambda_s-\lambda_{s'}:s,s'\in S\},\qquad K\equiv|\Omega|, \tag{58}$$

where Ω collects distinct frequencies. Here $\tilde{F}(\omega)$ denotes the exact Fourier coefficient in the finite Fourier expansion of $F(\eta)$, while $F_{\text{est}}(\cdot)$ will be reserved for shot-noise estimators obtained from finite sampling. Grouping identical frequencies yields a finite Fourier series

$$F(\eta) = \sum_{\omega\in\Omega} \tilde{F}(\omega) e^{i\omega\eta}, \qquad \tilde{F}(\omega) = \sum_{s,s':\lambda_s-\lambda_{s'}=\omega} \mathrm{Tr}[\boldsymbol{\rho}_0 P_s \mathbf{A}(t) P_{s'}]\,. \tag{59}$$

Consequently, the mth derivative of $F(\eta)$ at $\eta = 0$ is

$$F^{(m)}(0) = \sum_{\omega\in\Omega} \tilde{F}(\omega)(i\omega)^m. \tag{60}$$

GPSR as a linear system: a lower bound on the number of shifts

GPSR seeks shift points $\{s_p\}_{p=1}^M$ and coefficients $\{c_p^{(m)}\}_{p=1}^M$ such that

$$\boxed{F^{(m)}(0) = \sum_{p=1}^{M} c_p^{(m)} F(s_p).} \tag{61}$$

Substituting $F(s_p) = \sum_{\omega\in\Omega} \tilde{F}(\omega) e^{i\omega s_p}$ gives

$$\sum_{p=1}^{M} c_p^{(m)} F(s_p) = \sum_{\omega\in\Omega} \tilde{F}(\omega) \left(\sum_{p=1}^{M} c_p^{(m)} e^{i\omega s_p} \right). \tag{62}$$

For Eq. (A10) to hold for arbitrary Fourier amplitudes $\{\tilde{F}(\omega)\}$, one must satisfy, frequency by frequency,

$$\boxed{\sum_{p=1}^{M} e^{i\omega s_p} c_p^{(m)} = (i\omega)^m, \qquad \forall \omega \in \Omega.} \tag{63}$$

This linear system contains K independent constraints for M unknown coefficients. One can solve the coefficient $c_p^{(m)}$ classically if

$$\boxed{M \geq K = |\Omega|.} \tag{64}$$

In practice one often sets $M = K$ and chooses $\{s_p\}$ to improve the conditioning of the Vandermonde-type matrix $V_{\omega,p} = e^{i\omega s_p}$; the resulting coefficient norms directly control the sampling overhead.

B.2 Sampling complexity (shots) and coefficient-norm amplification

After solving the coefficient $c_p^{(m)}$, the mth derivative $F^{(m)}(0)$ can be obtained according to Eq. (61) with $F(s_p)$ estimated on quantum computers. Assume $F(s_p)$ is estimated from N_p shots by an unbiased estimator $F_{\text{est}}(s_p)$. The GPSR estimator is

$$F_{\text{est}}^{(m)}(0) = \sum_{p=1}^{M} c_p^{(m)} F_{\text{est}}(s_p). \tag{65}$$

Assuming independent sampling across shift points,

$$\mathrm{Var}\Big(F_{\text{est}}^{(m)}(0)\Big) = \sum_{p=1}^{M} (c_p^{(m)})^2 \,\mathrm{Var}(F_{\text{est}}(s_p))\,. \tag{66}$$

For bounded observables (e.g., Pauli outcomes ± 1), $\mathrm{Var}(F_{\mathrm{est}}(s_p)) \le 1/N_p$. Let $N_{\mathrm{tot}} = \sum_{p=1}^{M} N_p$ be the *total* number of shots across all shifts. Under uniform allocation $N_p = N_{\mathrm{tot}}/M$,

$$\mathrm{Var}\Big(F_{\mathrm{est}}^{(m)}(0)\Big) \le \frac{M\,\|c^{(m)}\|_2^2}{N_{\mathrm{tot}}}, \qquad \|c^{(m)}\|_2^2 \equiv \sum_{p=1}^{M} (c_p^{(m)})^2. \tag{67}$$

Therefore, to achieve an additive standard deviation ϵ, it suffices to take

$$\boxed{N_{\mathrm{tot}} \gtrsim \frac{M\,\|c^{(m)}\|_2^2}{\epsilon^2}.} \tag{68}$$

While the bounds above are exact, they are worst-case with respect to the choice of the pump generator $\mathbf{B}$. For a generic many-body operator $\mathbf{B}$ acting on a Hilbert space of dimension d with an essentially non-degenerate spectrum, the spectral-difference set may reach $|\Omega| = \Theta(d^2)$, implying that the number of required shifts can grow exponentially with system size. Therefore, GPSR-based measurements are efficient only under physically motivated restrictions on the pump operator.

In this work we restrict to physically implementable impulsive pumps, where each kick generator is a low-weight local operator, or a sum of commuting local terms supported on a region of size r (independent of, or at most polynomial in, the total system size N). A representative choice is

$$\mathbf{B} = \sum_{j \in \mathcal{S}} b_j, \qquad [b_j, b_{j'}] = 0, \qquad \|b_j\| = O(1), \qquad r \equiv |\mathcal{S}|. \tag{69}$$

In this setting, the spectrum of $\mathbf{B}$ is confined to an interval of width $O(r)$, and the number of distinct gaps satisfies

$$K = |\Omega| = O(r), \tag{70}$$

so exact reconstruction requires only $M = O(r)$ shift points (and $M = O(1)$ when $r = O(1)$).

Moreover, choosing Fourier-grid shifts $s_p = 2\pi(p-1)/M$ typically yields a well-conditioned reconstruction matrix (equivalently, a discrete Fourier transform over the gap set). One then obtains the rough scaling estimate

$$\|c^{(m)}\|_2^2 = O\left(\frac{1}{M} \sum_{\omega \in \Omega} |\omega|^{2m}\right) = O(r^{2m}), \tag{71}$$

which leads, for fixed derivative order m, to a polynomial total-shot requirement

$$N_{\mathrm{tot}} = O\left(\frac{M\|c^{(m)}\|_2^2}{\epsilon^2}\right) = O\left(\frac{r^{2m+1}}{\epsilon^2}\right). \tag{72}$$

In our exemplary models, each impulsive pump is generated by a single-site or two-site Pauli operator (or a short sum of commuting local terms), hence $r = O(1)$ and $K = O(1)$ (e.g., eigenvalues $\pm 1/2$ yield gaps $\Omega = \{2\}$). Accordingly, both the shift count M and the coefficient amplification $\|c^{(m)}\|_2$ remain bounded as the system size increases, justifying the efficiency claim in N at fixed response order.

This shows that the sampling cost is governed by both the shift count M and the coefficient amplification $\|c^{(m)}\|_2$, which depends on the spectral structure Ω and the conditioning of the reconstruction linear system. In typical physical settings with local (or commuting) pumps supported on r sites, one has $|\Omega| = O(r)$ and an exact GPSR reconstruction uses $M = O(r)$ shifts (in particular $M = O(1)$ when $r = O(1)$). For Fourier-grid shifts $s_p = 2\pi(p-1)/M$ and fixed derivative order m, the coefficient norm scales as $\|c^{(m)}\|_2^2 = O(r^{2m})$, leading to a polynomial shot complexity $N_{\mathrm{tot}} = O(r^{2m+1}/\epsilon^2)$. In our exemplary models, $\mathbf{B}$ is a one- or two-site Pauli operator (or a short commuting sum), hence $r = O(1)$ and both M and $\|c^{(m)}\|_2$ remain bounded with system size.

B.3 Multi-parameter GPSR: circuit count and factorized error bounds

We now consider L pump parameters $\vec{\eta} = (\eta_0, \ldots, \eta_{L-1})$ and a multi-index $\vec{\beta} = (\beta_0, \ldots, \beta_{L-1})$. For each direction a, GPSR uses M_a shifts $\{s_{a,p_a}\}_{p_a=1}^{M_a}$ and one-dimensional coefficients $\{c_{a,p_a}^{(\beta_a)}\}$.

Circuit instances: Cartesian product scaling

GPSR evaluates $\mathcal{G}_{\mathbf{A}}(\vec{\eta})$ on the Cartesian product grid

$$\vec{s}_{\vec{p}} = (s_{0,p_0}, \ldots, s_{L-1,p_{L-1}}), \qquad \vec{p} = (p_0, \ldots, p_{L-1}), \qquad p_a \in \{1, \ldots, M_a\}. \tag{73}$$

Hence the number of distinct circuit instances is

$$\boxed{N_{\text{circ}} = \prod_{a=0}^{L-1} M_a.} \tag{74}$$

If $\beta_a = 0$ (no derivative in direction a), one may set $M_a = 1$, giving

$$N_{\text{circ}} = \prod_{a \in \mathcal{A}} M_a, \qquad \mathcal{A} \equiv \{a : \beta_a > 0\}. \tag{75}$$

Moreover, applying the single-parameter argument to each $\mathbf{B}_a$ with its spectral-difference set Ω_a, exact reconstruction generically requires

$$\boxed{M_a \geq |\Omega_a| \quad \Rightarrow \quad N_{\text{circ}} \geq \prod_{a \in \mathcal{A}} |\Omega_a|.} \tag{76}$$

Factorized variance bounds: uniform and optimal shots

The multi-parameter GPSR estimator can be written as

$$\Xi_{\text{est}} = \sum_{\vec{p}} C_{\vec{p}}\, \mathcal{G}_{\mathbf{A},\text{est}}(\vec{s}_{\vec{p}}), \qquad C_{\vec{p}} = \prod_{a=0}^{L-1} c_{a,p_a}^{(\beta_a)}. \tag{77}$$

Assuming independent sampling across configurations $\vec{p}$,

$$\text{Var}(\Xi_{\text{est}}) = \sum_{\vec{p}} C_{\vec{p}}^2 \, \frac{\text{Var}_{\vec{p}}}{N_{\vec{p}}}. \tag{78}$$

c. (i) Uniform shots. If $\text{Var}_{\vec{p}} \leq 1$ and $N_{\vec{p}} = N_{\text{shot}}$ for all $\vec{p}$, then

$$\text{Var}(\Xi_{\text{est}}) \leq \frac{1}{N_{\text{shot}}} \sum_{\vec{p}} C_{\vec{p}}^2. \tag{79}$$

The product structure yields exact factorization,

$$\sum_{\vec{p}} C_{\vec{p}}^2 = \prod_{a=0}^{L-1} \left(\sum_{p_a=1}^{M_a} \left(c_{a,p_a}^{(\beta_a)} \right)^2 \right) = \prod_{a=0}^{L-1} \| c_a^{(\beta_a)} \|_2^2. \tag{80}$$

Thus a sufficient condition for precision ϵ is

$$\boxed{N_{\text{shot}} \gtrsim \frac{\prod_{a=0}^{L-1} \| c_a^{(\beta_a)} \|_2^2}{\epsilon^2}.} \tag{81}$$

The resulting total shot cost under uniform allocation is

$$\boxed{N_{\text{tot}} = N_{\text{circ}}\, N_{\text{shot}} \gtrsim \frac{\left(\prod_{a \in \mathcal{A}} M_a \right) \left(\prod_{a \in \mathcal{A}} \| c_a^{(\beta_a)} \|_2^2 \right)}{\epsilon^2}.} \tag{82}$$

d. (ii) Optimal shots under a fixed budget. If one allows non-uniform $N_{\vec{p}}$ under a fixed total budget $N_{\rm tot} = \sum_{\vec{p}} N_{\vec{p}}$, the variance is minimized by allocating

$$N_{\vec{p}} \propto |C_{\vec{p}}| \sqrt{\mathrm{Var}_{\vec{p}}}. \tag{83}$$

Under the conservative bound $\mathrm{Var}_{\vec{p}} \le 1$, one obtains

$$\sqrt{\mathrm{Var}_{\min}(\Xi_{\rm est})} \lesssim \frac{\sum_{\vec{p}} |C_{\vec{p}}|}{\sqrt{N_{\rm tot}}}. \tag{84}$$

Again, the ℓ_1 weight factorizes,

$$\sum_{\vec{p}} |C_{\vec{p}}| = \prod_{a=0}^{L-1} \left(\sum_{p_a=1}^{M_a} \left| c_{a,p_a}^{(\beta_a)} \right| \right) = \prod_{a=0}^{L-1} \| c_a^{(\beta_a)} \|_1. \tag{85}$$

Therefore, a sufficient condition for precision ϵ is

$$\boxed{N_{\rm tot} \gtrsim \frac{\left(\prod_{a=0}^{L-1} \| c_a^{(\beta_a)} \|_1 \right)^2}{\epsilon^2}.} \tag{86}$$

This bound is typically tighter than the uniform-allocation ℓ_2 bound.

B.4 Summary

The dominant GPSR resource scalings are controlled by: (i) the spectral-difference support $|\Omega_a|$ (lower bounding M_a), (ii) the Cartesian-product circuit count $N_{\rm circ} = \prod_{a \in \mathcal{A}} M_a$, and (iii) coefficient-norm amplification that governs shot complexity. In particular,

$$N_{\rm shot} \gtrsim \frac{\prod_a \| c_a^{(\beta_a)} \|_2^2}{\epsilon^2} \quad \text{(uniform allocation)}, \qquad N_{\rm tot} \gtrsim \frac{\left(\prod_a \| c_a^{(\beta_a)} \|_1 \right)^2}{\epsilon^2} \quad \text{(optimal allocation)}. \tag{87}$$

Finally, we emphasize that efficiency in the system size holds for fixed response order and physically implementable pumps (low-weight/local $\mathbf{B}_a$ or commuting sums on $O(1)$ support), for which $|\Omega_a|$ and the coefficient norms remain at most polynomial in N.

APPENDIX C: DIRECT CONSTRUCTION OF TIME- AND FREQUENCY-DOMAIN RESPONSE FUNCTIONS

For completeness, beyond the GPSR-based estimator and interpolation baseline, we also implemented a direct extraction of response functions; however, this approach is inferior to PSR and is only reliable when the perturbation strength η is carefully chosen, which severely limits its applicability.

As a baseline method for response extraction, we directly computed the first-order response function $\chi^{(1)}(t)$ from experimental measurements of the observable $\langle \mathbf{A}(t) \rangle_\eta$ at various perturbation strengths η. The linear response was estimated by rescaling the signal at finite η and subtracting the zero-field background. Specifically, we used

$$\chi^{(1)}(t) \approx \frac{\langle \mathbf{A}(t) \rangle_{s_1} - \langle \mathbf{A}(t) \rangle_0}{s_1}, \tag{88}$$

for a small but finite s_1. Time-domain profiles for $\chi^{(1)}(t)$ at different η values were compared against noiseless simulations.

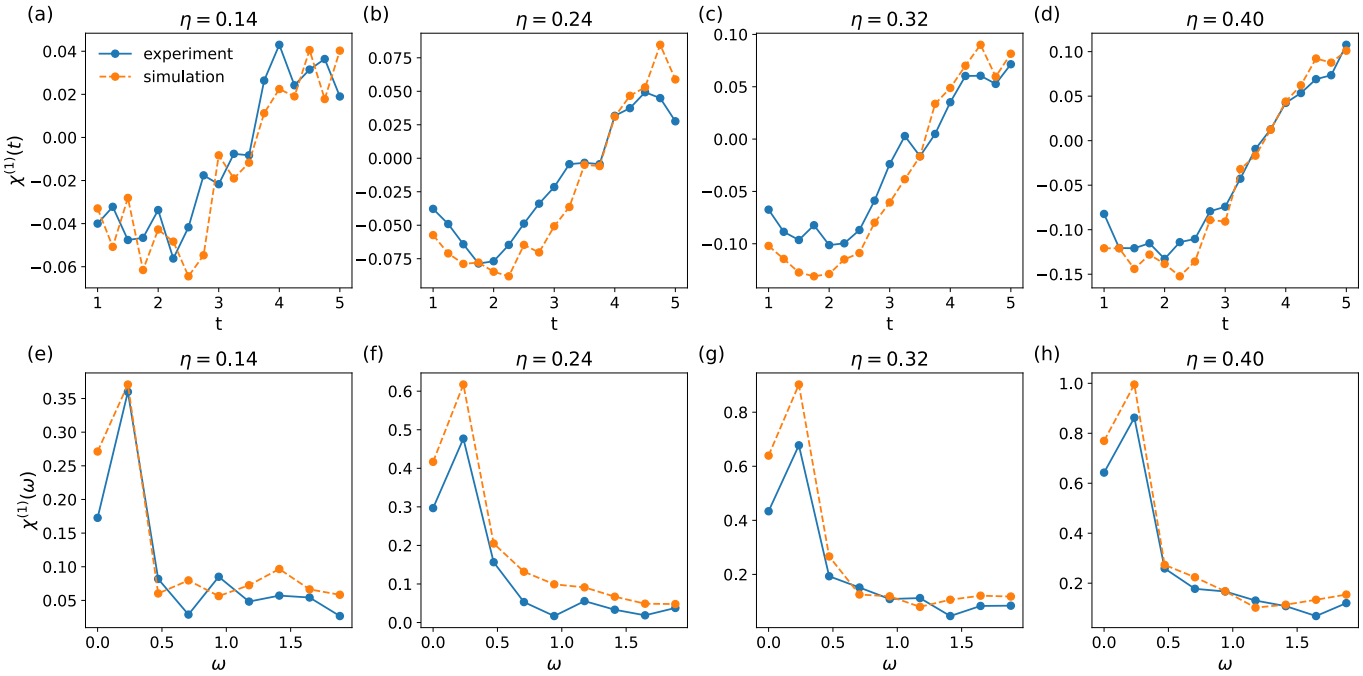

FIG. 6. First-order response functions $\chi^{(1)}(t)$ and $\chi^{(1)}(\omega)$ at various perturbation strengths. Panels (a)–(d) show the time-domain signals at $\eta = 0.14$, 0.24, 0.32, and 0.40, respectively. Panels (e)–(h) present the corresponding frequency-domain spectra. Blue lines denote experimental results; orange dashed lines correspond to noiseless simulations. In the low η regime (e.g., $\eta = 0.14$), larger fluctuations are observed due to lower signal-to-noise ratio, whereas the agreement improves significantly for larger η, illustrating the robustness of linear-response extraction at moderate perturbation strengths.

Beyond the linear term, we also employed a stepwise signal decomposition in the spirit of standard response theory. We assume a power-series expansion of the pump-dependent signal,

$$\langle \mathbf{A}(t)\rangle_\eta \approx A^0(t) + \eta\, A^1(t) + \eta^3 A^3(t) + \eta^5 A^5(t) + \cdots , \tag{89}$$

where $A^n(t)$ collects the n-th order contribution to the response (with odd orders selected by symmetry in our setup). Given measurements at several pump amplitudes s_1, s_2, s_3 in a perturbative window, one can regard

$$\begin{pmatrix} \langle \mathbf{A}(t)\rangle_{s_1} - \langle \mathbf{A}(t)\rangle_0 \\ \langle \mathbf{A}(t)\rangle_{s_2} - \langle \mathbf{A}(t)\rangle_0 \\ \langle \mathbf{A}(t)\rangle_{s_3} - \langle \mathbf{A}(t)\rangle_0 \end{pmatrix} \approx \begin{pmatrix} s_1 & s_1^3 & s_1^5 \\ s_2 & s_2^3 & s_2^5 \\ s_3 & s_3^3 & s_3^5 \end{pmatrix} \begin{pmatrix} A^1(t) \\ A^3(t) \\ A^5(t) \end{pmatrix} , \tag{90}$$

and solve this 3×3 linear system for $A^1(t)$, $A^3(t)$, and $A^5(t)$. In practice, instead of explicitly inverting the matrix, we use analytically simplified combinations that successively cancel lower-order terms.

To isolate the third-order component, we define

$$\tilde{A}_3(t) = \langle \mathbf{A}(t)\rangle_{s_2} - \frac{s_2}{s_1}\langle \mathbf{A}(t)\rangle_{s_1}, \tag{91}$$

which eliminates the leading linear term and leaves a dominant third-order signal proportional to $A^3(t)$, up to higher-order corrections. The corresponding third-order response function $\chi^{(3)}(\omega)$ is obtained by taking the discrete Fourier transform of $\tilde{A}_3(t)$ and applying a suitable normalization.

For the fifth-order term, we perform one more subtraction step:

$$\tilde{A}_5(t) = \langle \mathbf{A}(t)\rangle_{s_3} - \frac{s_3}{s_1}\langle \mathbf{A}(t)\rangle_{s_1} - \left(\frac{s_3^3}{s_2^3}\right)\left[\langle \mathbf{A}(t)\rangle_{s_2} - \frac{s_2}{s_1}\langle \mathbf{A}(t)\rangle_{s_1}\right]. \tag{92}$$

This expression cancels both the linear and third-order contributions under the polynomial ansatz, leaving a residual signal dominated by $s_3^5 A^5(t)$, from which the fifth-order response $A^5(t)$ and its Fourier transform $\chi^{(5)}(\omega)$ can be extracted.

The extracted responses $\chi^{(1)}(t)$, $\chi^{(3)}(t)$, and $\chi^{(5)}(t)$, as well as their corresponding Fourier spectra, are shown in Fig. 7 for the representative case of $\eta = 0.40$. These results demonstrate how higher-order contributions and the associated nonlinear spectra can be resolved by combining measurements at multiple pump strengths under a controlled power-series expansion.

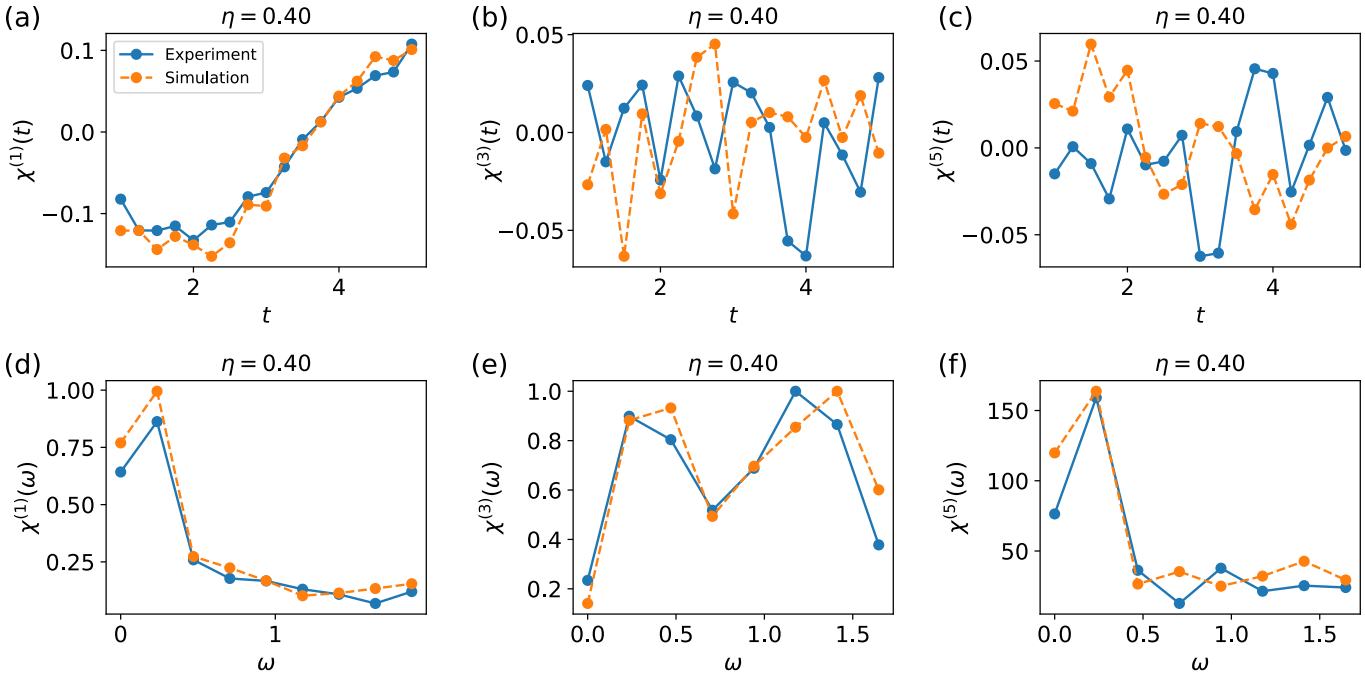

FIG. 7. Time- and frequency-domain nonlinear response functions at $\eta = 0.40$, computed using the direct subtraction method. (a)–(c) show the time-domain responses $\chi^{(1)}(t)$, $\chi^{(3)}(t)$, and $\chi^{(5)}(t)$, obtained by successively removing lower-order contributions from raw signals. (d)–(f) present the corresponding frequency-domain spectra $\chi^{(1)}(\omega)$, $\chi^{(3)}(\omega)$, and $\chi^{(5)}(\omega)$ via discrete Fourier transform. Solid blue lines denote experimental results, and dashed orange lines represent noiseless simulations. While the main low-frequency structures are captured, higher-order components suffer from visible fluctuations, especially in the time domain.

Overall, the direct finite-difference and stepwise subtraction methods provide a conceptually simple, response-theory–style route to constructing time- and frequency-domain response functions. However, their performance is limited by the choice of η and by noise amplification at higher orders.

APPENDIX D: RESPONSE FUNCTION OF MAGNETIZATION

In the study of quantum many-body systems, the evaluation of magnetization plays a central role in probing the dynamic response of a spin system to external perturbations. This work focuses on the calculation of magnetization in the x-direction, denoted $\langle M^x(t)\rangle$, within a finite quantum spin chain governed by an XXZ Hamiltonian with a static, spatially modulated transverse field.

The unperturbed Hamiltonian of the system is defined as

$$\mathbf{H}_0 = \frac{1}{4}\sum_{j=0}^{N-2}\left(X_jX_{j+1} + Y_jY_{j+1} + \Delta Z_jZ_{j+1}\right) - \frac{h_e}{2}\sum_{j=0}^{N-1} Z_j, \tag{93}$$

where X_j, Y_j, Z_j are Pauli operators acting on site j, Δ is the anisotropy parameter, h_e is the longitudinal magnetic field strength, and N is the total number of spins. A transverse perturbation is introduced in the form

$$\mathbf{B} = \sum_{j=0}^{N-1}\cos\left(\frac{2\pi j}{N}\right)X_j, \tag{94}$$

and the full Hamiltonian becomes

$$\mathbf{H} = \mathbf{H}_0 + \eta \mathbf{B}, \tag{95}$$

where η denotes the perturbation strength.

The observable of interest is the transverse magnetization per site, defined as

$$\mathbf{M}^x = -\frac{1}{N} \sum_{j=0}^{N-1} X_j. \tag{96}$$

This operator captures the average spin alignment along the x-axis. The ground state $|\psi_0\rangle$ of the full Hamiltonian $\mathbf{H}$ is obtained through exact diagonalization, and the time-evolved state is given by

$$|\psi(t)\rangle = U(t)|\psi_0\rangle, \quad U(t) = e^{-i\mathbf{H}t}. \tag{97}$$

The time-dependent magnetization is then computed as the quantum expectation value

$$\langle M^x(t)\rangle = \langle \psi(t)|\mathbf{M}^x|\psi(t)\rangle. \tag{98}$$

Numerically, this is evaluated by

$$\langle M^x(t)\rangle = \mathrm{Re}\left[\psi(t)^\dagger \mathbf{M}^x \psi(t)\right], \tag{99}$$

where $\psi(t) \in \mathbb{C}^{2^N}$ and $\mathbf{M}^x$ is the corresponding Hermitian matrix operator.

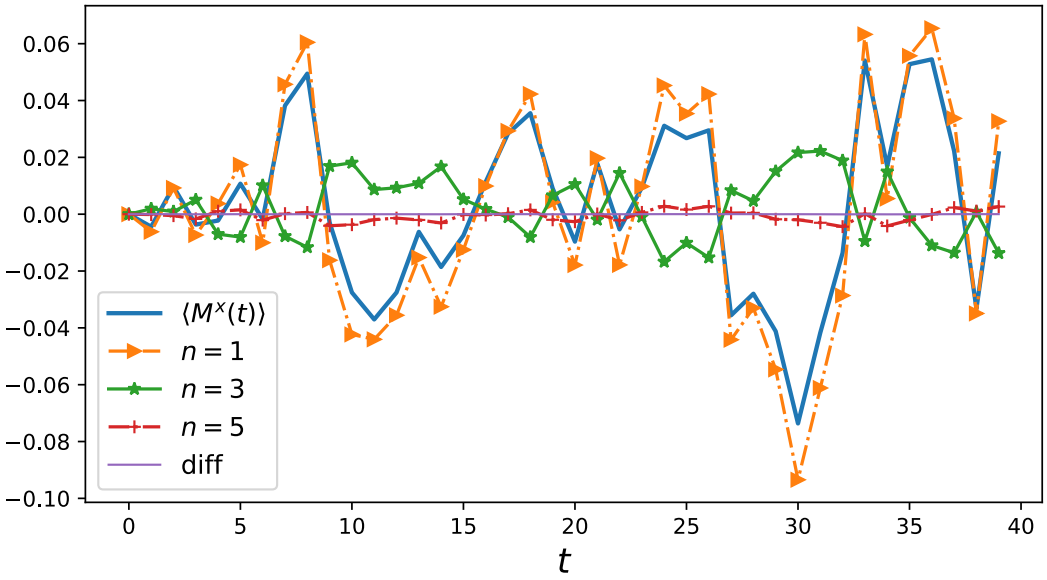

FIG. 8. Magnetization signal $\langle M^x(t)\rangle_\eta$ and its extracted response contributions in the η expansion. The $n = 0$ term corresponds to the unpumped baseline $\langle M^x(t)\rangle_{\eta=0}$. Due to symmetry, the even-order contributions (e.g., $n = 2, 4$) vanish within numerical precision, and we display the leading nonzero odd orders ($n = 1, 3, 5$). The curve labeled "diff" denotes the residual between the measured $\langle M^x(t)\rangle_\eta$ and the reconstructed partial sum obtained by adding the retained (nonzero) response contributions together with the $n = 0$ baseline, serving as a consistency check.

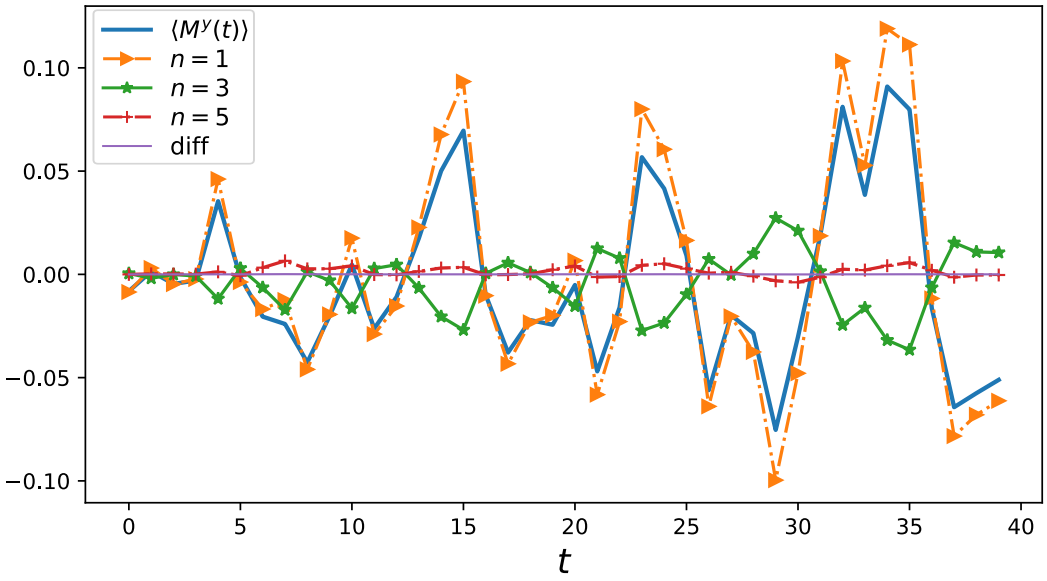

FIG. 9. Magnetization signal $\langle M^y(t)\rangle_\eta$ and its extracted response contributions in the η expansion. The $n = 0$ term corresponds to the unpumped baseline $\langle M^y(t)\rangle_{\eta=0}$. Due to symmetry, the even-order contributions (e.g., $n = 2, 4$) vanish within numerical precision, and we display the leading nonzero odd orders ($n = 1, 3, 5$). The curve labeled "diff" denotes the residual between the measured $\langle M^y(t)\rangle_\eta$ and the reconstructed partial sum obtained by adding the retained (nonzero) response contributions together with the $n = 0$ baseline, serving as a consistency check.

To study nonlinear effects, the magnetization is expanded as a power series in η using nested commutators. Assuming the dynamics are governed by the unperturbed evolution operator $U_0(t) = e^{-i\mathbf{H}_0 t}$ and the observable in the Heisenberg picture is $\mathbf{M}^x(t) = U_0^\dagger(t)\mathbf{M}^x U_0(t)$, the expansion takes the form

$$\langle \mathbf{M}^x(t)\rangle_\eta = \langle \mathbf{M}^x(t)\rangle_0 + i\eta\langle[\mathbf{B}, \mathbf{M}^x(t)]\rangle_0 + \frac{(i\eta)^2}{2!}\langle[\mathbf{B}, [\mathbf{B}, \mathbf{M}^x(t)]]\rangle_0 + \frac{(i\eta)^3}{3!}\langle[\mathbf{B}, [\mathbf{B}, [\mathbf{B}, \mathbf{M}^x(t)]]]\rangle_0 + \cdots, \tag{100}$$

where the expectation values are taken with respect to the ground state of $\mathbf{H}_0$. In practice, this expansion is carried out up to the seventh order to isolate linear and higher-order nonlinear contributions. The framework provides a comprehensive way to characterize dynamical response functions and can be extended to other forms of quantum perturbation theory. Illustrative results for the magnetization dynamics and the associated higher-order contributions are presented in Fig. 8 to Fig. 9.

APPENDIX E: RESPONSE FUNCTION OF SPIN-SPIN CORRELATION FUNCTION

To characterize the spatial and dynamical correlations in the quantum spin chain, we compute the two-point and four-point spin correlation functions in various directions. The two-point spin correlation function between sites i and j along directions α and β is defined as

$$C_{i,j}^{\alpha\beta}(t) = \langle\psi(t)|P_i^\alpha P_j^\beta|\psi(t)\rangle, \tag{101}$$

where P_i^α and P_j^β are Pauli operators acting on sites i and j in directions $\alpha, \beta \in \{x, y, z\}$ respectively, and $|\psi(t)\rangle$ denotes the time-evolved state of the system under the full Hamiltonian $\mathbf{H}$. These quantities reflect the quantum correlations between different spin components and are sensitive to the anisotropy and external field parameters of the system. For instance, the $C_{0,1}^{xx}(t)$ correlation quantifies the alignment tendency between the x components of neighboring spins at sites 0 and 1, and its temporal evolution provides insight into the propagation of local perturbations and collective excitations.

The evaluation is implemented numerically by representing the spin operators as tensor products of Pauli matrices and identity matrices in the full 2^N-dimensional Hilbert space. Given the state vector $\psi(t)$ at time t, the correlation is computed as

$$C_{i,j}^{\alpha\beta}(t) = \mathrm{Re}\left[\psi(t)^\dagger (P_i^\alpha P_j^\beta)\psi(t)\right], \tag{102}$$

where the operator $P_i^\alpha P_j^\beta$ is constructed via Kronecker products with appropriate identities acting on unaffected qubits. This method allows straightforward generalization to arbitrary spin directions and distances.

In addition to two-point correlations, higher-order correlations are also calculated to probe more complex quantum interactions and entanglement patterns. Specifically, we consider the four-point spin correlation function of the form

$$C_{i,j,k,l}^{\alpha\beta\gamma\delta}(t) = \langle\psi(t)|P_i^\alpha P_j^\beta P_k^\gamma P_l^\delta|\psi(t)\rangle, \tag{103}$$

with $\alpha, \beta, \gamma, \delta \in \{x, y, z\}$. As a representative example, the correlation $C_{0,1,2,3}^{xyxz}(t)$ involves spin operators along different directions and spatial locations, capturing intricate multi-body quantum correlations that are not accessible via two-point functions alone.

These multi-spin correlators are particularly important for identifying quantum phase transitions, topological order, or signatures of many-body localization. Their implementation follows the same principle: constructing the tensor product of four Pauli operators at the specified sites and evaluating the real part of the expectation value with the time-evolved state. The resulting data, resolved in time, reveals the interplay between spin components and the emergence of collective behavior under unitary dynamics.

This framework provides a versatile and numerically exact method for exploring both linear and nonlinear quantum correlations in finite spin systems and lays the foundation for studying dynamical structure factors, response functions, and entanglement growth in driven quantum systems. Detailed results for the two-point and four-point spin correlation functions, along with their higher-order effects, are shown in Fig. 10 $\sim$ Fig. 12.

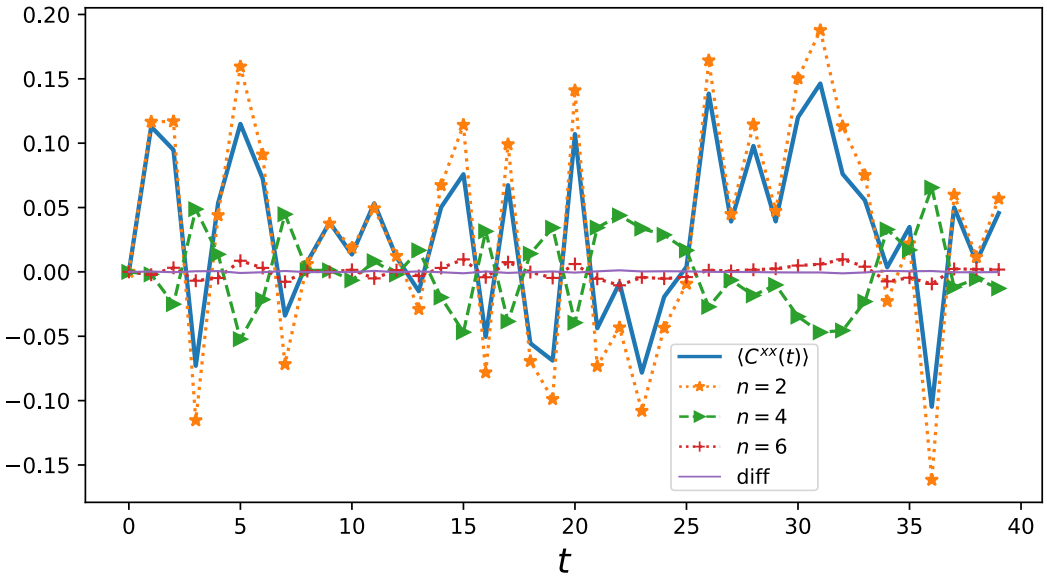

FIG. 10. Two-point correlation signal $\langle C^{xx}(t)\rangle_\eta$ and its extracted response contributions in the η expansion. The $n = 0$ term corresponds to the unpumped baseline $\langle C^{xx}(t)\rangle_{\eta=0}$. Due to symmetry, the odd-order contributions vanish within numerical precision, and we display the leading nonzero even orders ($n = 2, 4, 6$). The curve labeled "diff" denotes the residual between the measured $\langle C^{xx}(t)\rangle_\eta$ and the reconstructed partial sum obtained by adding the retained (nonzero) response contributions together with the $n = 0$ baseline, serving as a consistency check of the decomposition.

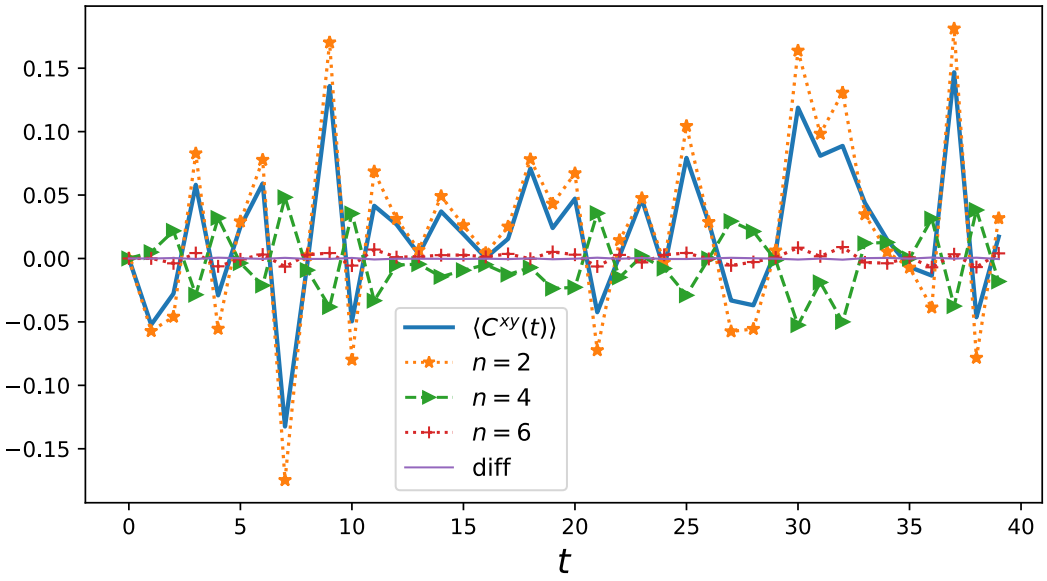

FIG. 11. Two-point correlation signal $\langle C^{xy}(t)\rangle_\eta$ and its extracted response contributions in the η expansion. The $n = 0$ term corresponds to the unpumped baseline $\langle C^{xy}(t)\rangle_{\eta=0}$. Due to symmetry, the odd-order contributions vanish within numerical precision, and we display the leading nonzero even orders ($n = 2, 4, 6$). The curve labeled "diff" denotes the residual between the measured $\langle C^{xy}(t)\rangle_\eta$ and the reconstructed partial sum obtained by adding the retained (nonzero) response contributions together with the $n = 0$ baseline, validating the fidelity of the decomposition.

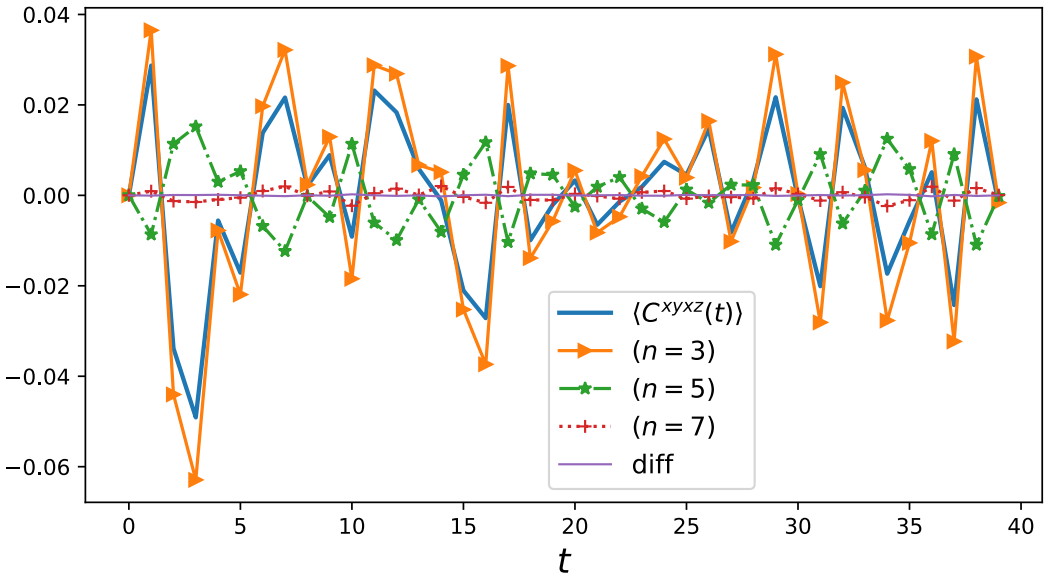

FIG. 12. Four-point correlation signal $\langle C^{xyxz}(t)\rangle_\eta$ and its extracted response contributions in the η expansion. The $n = 0$ term corresponds to the unpumped baseline $\langle C^{xyxz}(t)\rangle_{\eta=0}$. Due to symmetry, the even-order contributions vanish within numerical precision, and we display the leading nonzero odd orders ($n = 3, 5, 7$). The curve labeled "diff" denotes the residual between the measured $\langle C^{xyxz}(t)\rangle_\eta$ and the reconstructed partial sum obtained by adding the retained (nonzero) response contributions together with the $n = 0$ baseline, confirming the correctness of the computed decomposition.

APPENDIX F: RESPONSE FUNCTION OF CURRENT DENSITY

To investigate the dynamical transport properties of the spin chain, we evaluate the spin current operators along various directions. In quantum spin systems, the spin current between two adjacent sites i and j in direction $a \in \{x, y, z\}$ is generally defined through the continuity equation for spin density and takes the form of an antisymmetric combination of local spin operators. Specifically, the spin current operator along the x-direction is given by

$$J^x_{s,ij} = Y_i Z_j - Z_i Y_j, \tag{104}$$

where X_i, Y_i, Z_i denotes the Pauli operator acting on site i in the corresponding direction. Similarly, the spin current in the y- and z-directions is constructed by cyclic permutation of the Pauli matrices:

$$J^y_{s,ij} = Z_i X_j - X_i Z_j, \tag{105}$$

$$J^z_{s,ij} = X_i Y_j - Y_i X_j. \tag{106}$$

These operators represent the flow of spin angular momentum between neighboring sites and are key observables in characterizing transport, dissipation, and symmetry breaking in spin systems.

In our numerical implementation, the spin current operator is encoded as a $2^N \times 2^N$ Hermitian matrix constructed via Kronecker products of the Pauli matrices and identity operators, such that the relevant operators act non-trivially only on sites i and j. For a given time t, the quantum state of the system is evolved under the full Hamiltonian $\mathbf{H}$ from an initial ground state $|\psi_0\rangle$, resulting in

$$|\psi(t)\rangle = e^{-i\mathbf{H}t}|\psi_0\rangle. \tag{107}$$

The time-dependent expectation value of the spin current is then computed as

$$\langle J^a_{s,ij}(t)\rangle = \langle\psi(t)|J^a_{s,ij}|\psi(t)\rangle, \tag{108}$$

and in practice is evaluated numerically as

$$\langle J^a_{s,ij}(t)\rangle = \mathrm{Re}\left[\psi(t)^\dagger J^a_{s,ij}\psi(t)\right]. \tag{109}$$

In order to characterize the overall strength of the spin transport, we report the absolute value of this expectation value:

$$|\langle J^a_{s,ij}(t)\rangle|. \tag{110}$$

This measure reflects the instantaneous magnitude of spin flow, independent of its direction.

To further resolve the nonlinear contributions of spin transport under a modulated transverse field, we adopt a commutator-based expansion of the expectation value with respect to the perturbation strength η. For the unperturbed Hamiltonian $\mathbf{H}_0$ and corresponding time evolution operator $U_0(t) = e^{-i\mathbf{H}_0 t}$, the observable in the Heisenberg picture is

$$J^a_{s,ij}(t) = U_0^\dagger(t) J^a_{s,ij} U_0(t), \tag{111}$$

and its perturbative expansion in η takes the form

$$\begin{aligned}\langle J^a_{s,ij}(t)\rangle_\eta = \langle J^a_{s,ij}(t)\rangle_0 + i\eta\langle[\mathbf{B}, J^a_{s,ij}(t)]\rangle_0 + \frac{(i\eta)^2}{2!}\langle[\mathbf{B},[\mathbf{B}, J^a_{s,ij}(t)]]\rangle_0 \\ + \frac{(i\eta)^3}{3!}\langle[\mathbf{B},[\mathbf{B},[\mathbf{B}, J^a_{s,ij}(t)]]]\rangle_0 + \cdots,\end{aligned} \tag{112}$$

where $\mathbf{B}$ is the transverse perturbation operator and the expectation values are taken with respect to the ground state of $\mathbf{H}_0$. This expansion allows for the decomposition of the observed current into linear and higher-order nonlinear contributions, enabling the identification of resonant response, symmetry-induced cancellations, and nontrivial transport dynamics beyond linear response.

The resulting spin current data, resolved in both time and perturbation order, serve as a diagnostic of the system's dynamical behavior under driving, and provide a route to extracting transport coefficients and collective phenomena in strongly interacting spin models. Detailed results for the spin current, along with their higher-order effects, are shown in Fig. 13 $\sim$ Fig. 15.

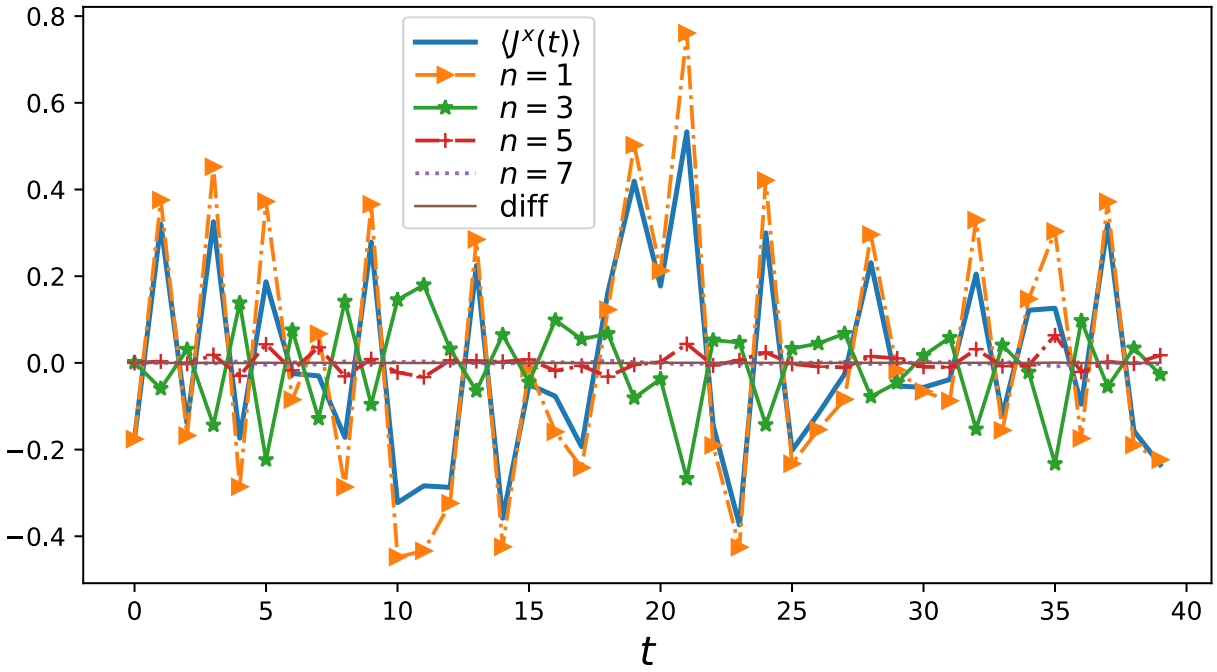

FIG. 13. Current-density signal $\langle J^x(t)\rangle_\eta$ and its extracted response contributions in the η expansion. The $n = 0$ term corresponds to the unpumped baseline $\langle J^x(t)\rangle_{\eta=0}$. Due to symmetry, the even-order contributions vanish within numerical precision, and we display the leading nonzero odd orders ($n = 1, 3, 5, 7$). The curve labeled "diff" denotes the residual between the measured $\langle J^x(t)\rangle_\eta$ and the reconstructed partial sum obtained by adding the retained (nonzero) response contributions together with the $n = 0$ baseline, serving as a consistency check.

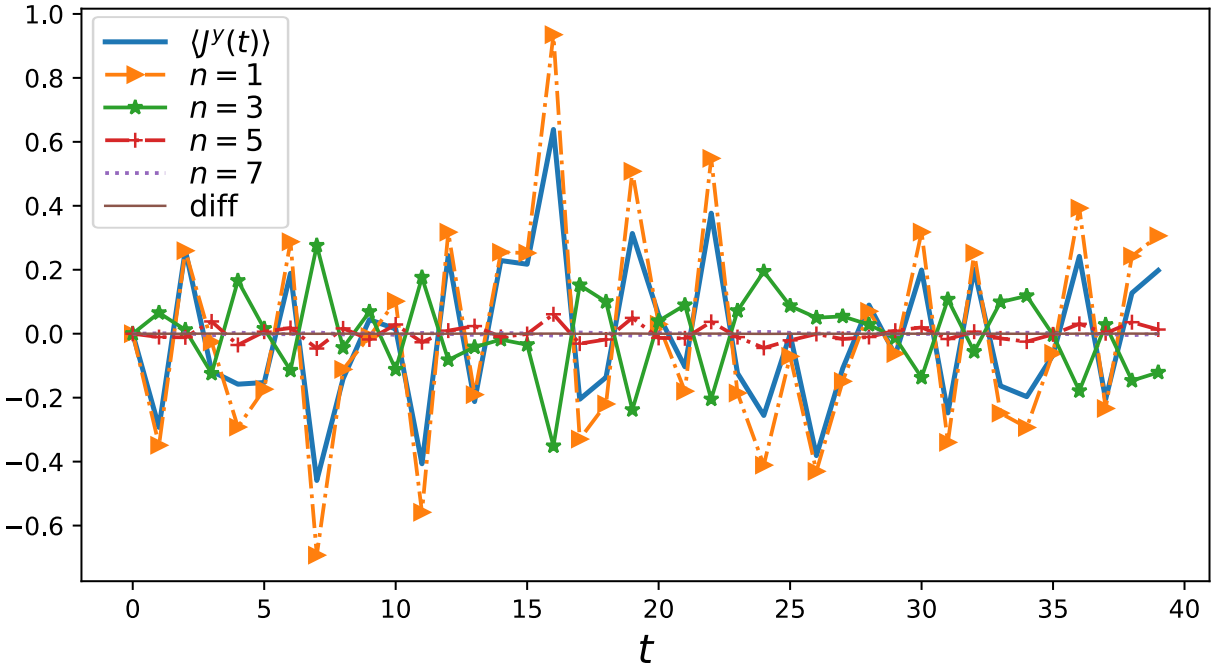

FIG. 14. Current-density signal $\langle J^y(t)\rangle_\eta$ and its extracted response contributions in the η expansion. The $n = 0$ term corresponds to the unpumped baseline $\langle J^y(t)\rangle_{\eta=0}$. Due to symmetry, the even-order contributions vanish within numerical precision, and we display the leading nonzero odd orders ($n = 1, 3, 5, 7$). The curve labeled "diff" denotes the residual between the measured $\langle J^y(t)\rangle_\eta$ and the reconstructed partial sum obtained by adding the retained (nonzero) response contributions together with the $n = 0$ baseline, serving as a consistency check.

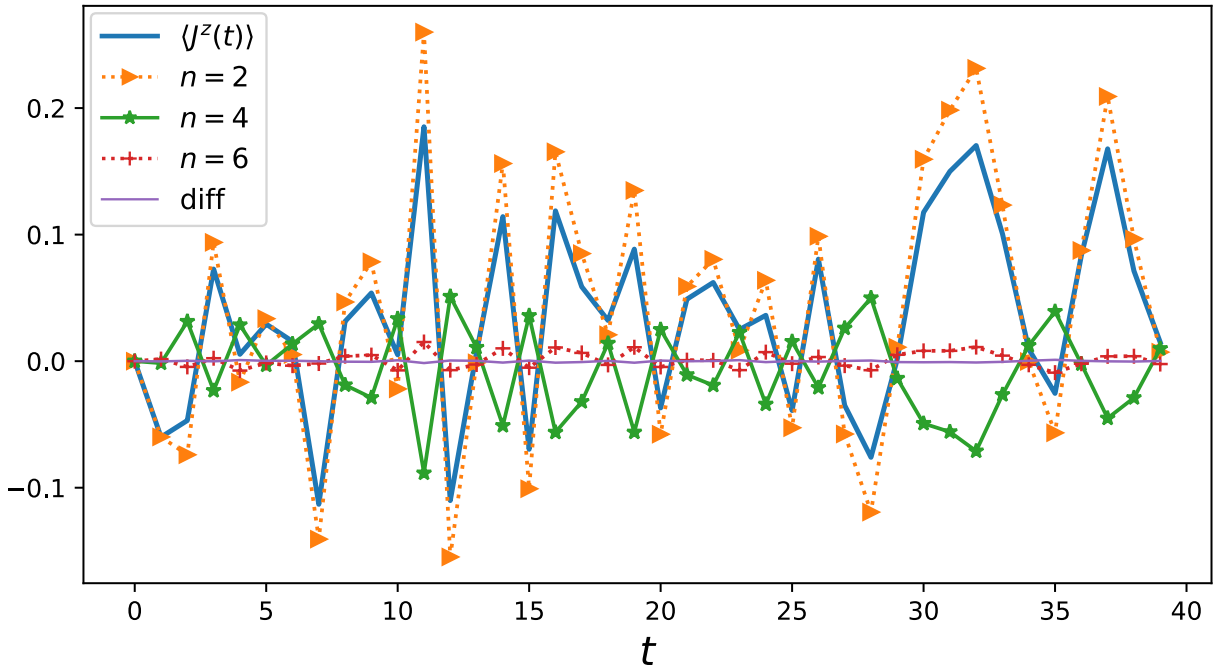

FIG. 15. Current-density signal $\langle J^z(t)\rangle_\eta$ and its extracted response contributions in the η expansion. The $n = 0$ term corresponds to the unpumped baseline $\langle J^z(t)\rangle_{\eta=0}$. Due to symmetry, the odd-order contributions vanish within numerical precision, and we display the leading nonzero even orders ($n = 2, 4, 6$). The curve labeled "diff" denotes the residual between the measured $\langle J^z(t)\rangle_\eta$ and the reconstructed partial sum obtained by adding the retained (nonzero) response contributions together with the $n = 0$ baseline, serving as a consistency check.

APPENDIX G: SCHEME FOR DETECTING QUASI-PARTICLE EXCITATIONS VIA RESPONSE FUNCTION

In addition to the mixed-field operator

$$\mathbf{B} = \sum_{i=0}^{N-1} (X_i + Z_i), \tag{113}$$

we also explored alternative forms of the perturbation operator $\mathbf{B}$ across different models. In the XXZ spin chain, we considered a purely transverse field perturbation,

$$\mathbf{B} = \sum_{i=0}^{N-1} X_i, \tag{114}$$

which still yields a well-defined quasi-particle spectrum with identifiable linear response contributions.

For the Kitaev honeycomb model, the operator

$$\mathbf{B} = \sum_{i=0}^{N-1} Y_i \tag{115}$$

was used to probe spin dynamics along the y-direction, which is naturally aligned with one of the anisotropic bond interactions in the model. Despite the model's topological nature, we observed that this form of $\mathbf{B}$ also produces clear linear response features in the time-domain signals.

In the case of the 2D toric code (Kitaev toric model), we adopted a generalized operator acting on a set of plaquette sites:

$$\mathbf{B} = \sum_{i \in \text{sites}} Y_i, \tag{116}$$

which targets the creation and propagation of localized flux excitations. Remarkably, all these choices of **B** lead to nontrivial linear response behavior, suggesting that the linear components of the quasi-particle spectrum are robust features across various models and operator types. This highlights the universality of time-domain response techniques in capturing spectral signatures.

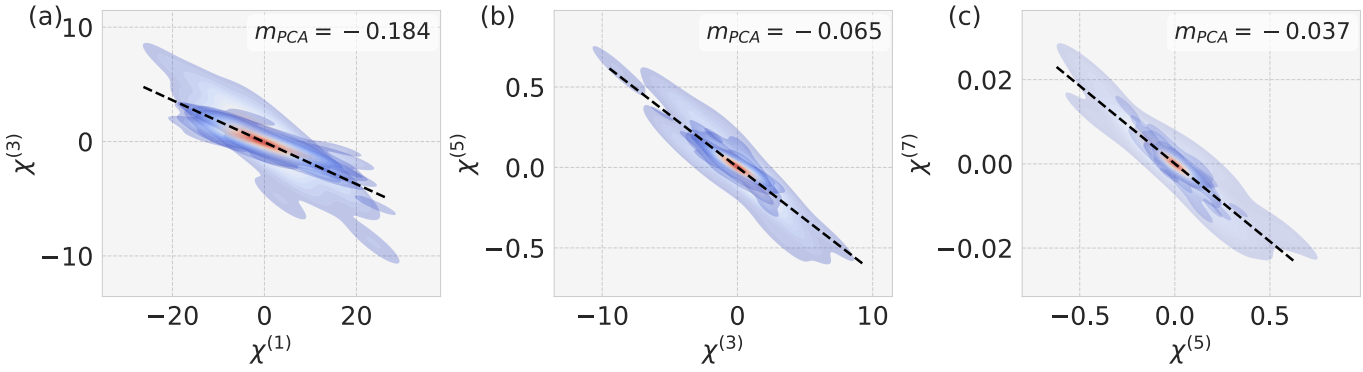

FIG. 16. Excitation spectrum of the XXZ model under a purely transverse field perturbation (Eq. 114). The corresponding response function exhibits a clear linear trend, with m_{PCA} denoting the fitted slope obtained via principal component analysis.

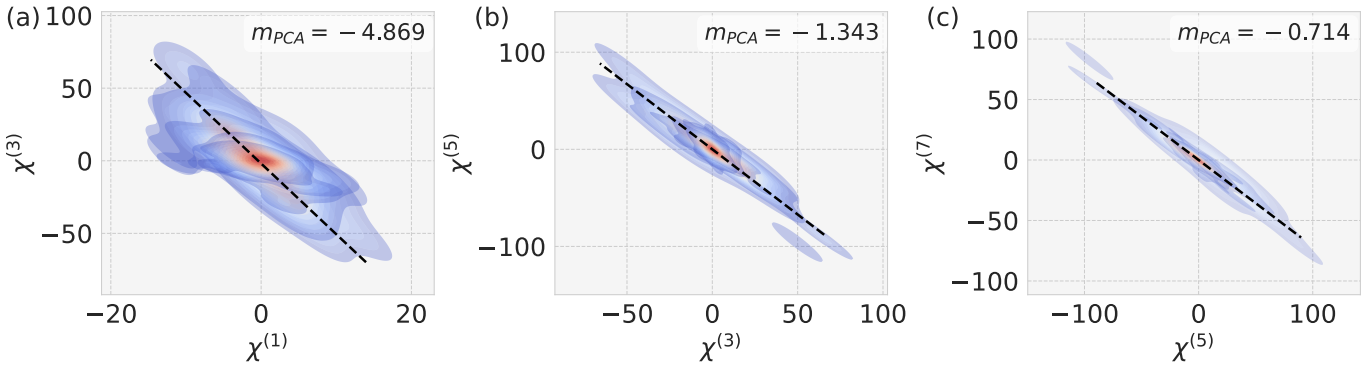

FIG. 17. Excitation spectrum of the Kitaev honeycomb model subject to a purely transverse field perturbation (Eq. 115). The response function maintains a well-defined linear dependence, and m_{PCA} represents the slope extracted through principal component fitting.

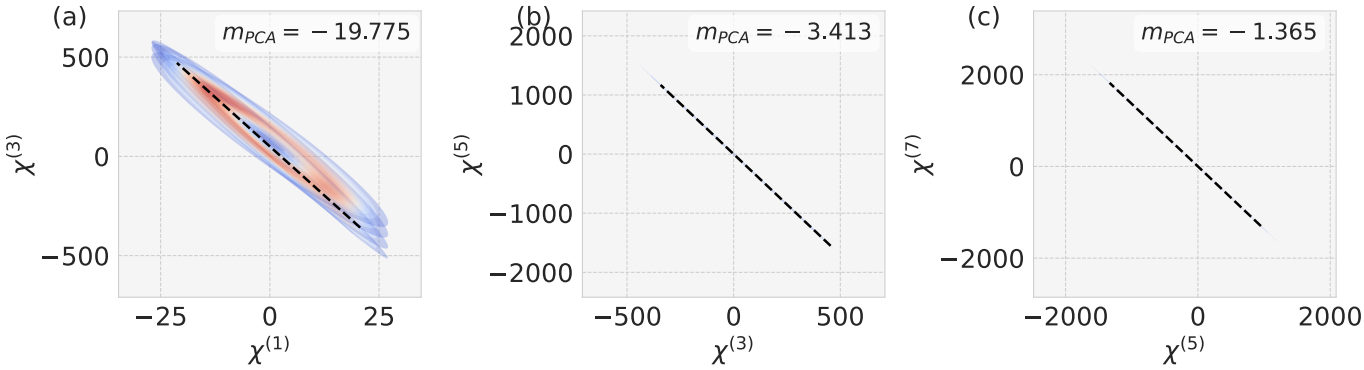

FIG. 18. Excitation spectrum of the Kitaev toric code model under the application of a purely transverse field perturbation (Eq. 116). The response function displays a pronounced linear relationship, with m_{PCA} indicating the slope obtained from principal component analysis.

Future work will focus on a systematic comparison of quasi-particle excitation spectra across various models, parameter regimes, and distinct quantum phases to uncover model-dependent behaviors and phase-specific spectral

signatures. In summary, this appendix collects the minimal technical details behind our response-extraction pipeline. We show how multi-time, higher-order response coefficients can be written as derivatives of a pulse-amplitude generating function and then evaluated exactly from a finite set of shifted circuits via the GPSR. Different observables can obey different symmetry selection rules, so the set of nonzero response orders may vary across the plots, while the "diff" curve serves as a practical consistency check of the reconstruction. Looking ahead, it would be useful to optimize the choice of shift points and measurement budget to further improve the stability of higher-order components under finite-shot noise.